Supplementary information

Optoelectronic synapses with chemical-electric behaviors in gallium nitride semiconductors for biorealistic neuromorphic functionality

Xin Liu[1,5], Danhao Wang[1,5], Wei Chen[1,5], Yang Kang[1], Shi Fang[1], Yuanmin Luo[1], Dongyang Luo[1], Huabin Yu[1], Haochen Zhang[1], Kun Liang[1], Lan Fu[2], Boon S. Ooi[3], Sheng Liu[4], Haiding Sun[1]*

[1]iGaN Laboratory, School of Microelectronics, University of Science and Technology of China, Hefei, Anhui 230026, China.

[2]Department of Electronic Materials Engineering, Research School of Physics and Engineering, The Australian National University, Canberra, ACT 2601, Australia.

[3]Computer, Electrical, and Mathematical Sciences and Engineering Division, King Abdullah University of Science and Technology, Thuwal 23955-6900, Saudi Arabia.

[4]The Institute of Technological Sciences, Wuhan University, Wuhan, Hubei 430072, China.

[5]These authors contributed equally: Xin Liu, Danhao Wang, Wei Chen.

*Corresponding author: haiding@ustc.edu.cn

Supplementary Note 1. Brief introduction on the photoelectrochemical architecture

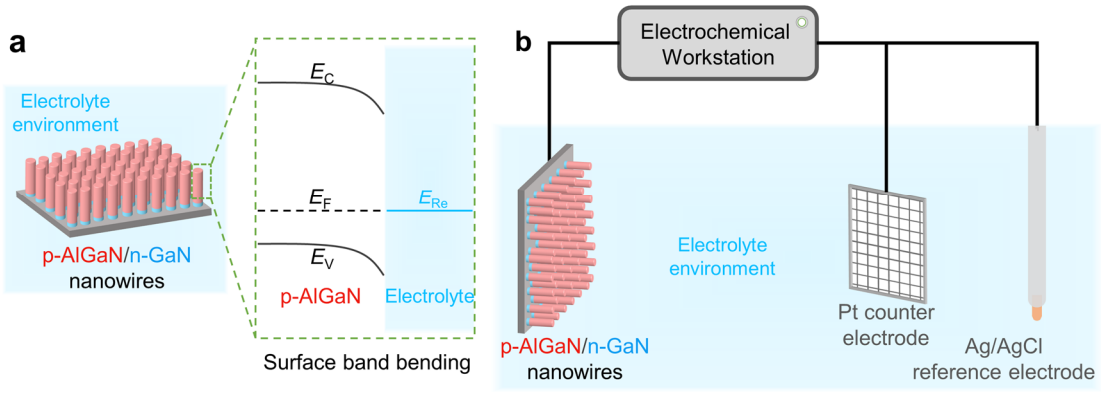

Supplementary Figure 1. Schematic illustration of the photoelectrochemical device. (a) Schematic illustration of surface band bending at the nanowire/electrolyte interface. (b) Schematic of a photoelectrochemical device based on three-electrode configuration.

Considering that the heterojunction nanowires mainly consist of p-AlGaN segment, when the p-AlGaN comes into contact with the electrolyte, due to the electrochemical equilibrium between the semiconductor and the electrolyte[1], the p-AlGaN presents a downward surface band bending at the nanowire/electrolyte interface (Supplementary Figure 1a). For photoelectrochemical devices, the three-electrode configuration is typically applied for performance assessments, which comprises the nanowire photoelectrode, Pt counter electrode, and Ag/AgCl reference electrode. It is worth noting that Figure 2b presents a simplified illustration of the device structure without the reference electrode.

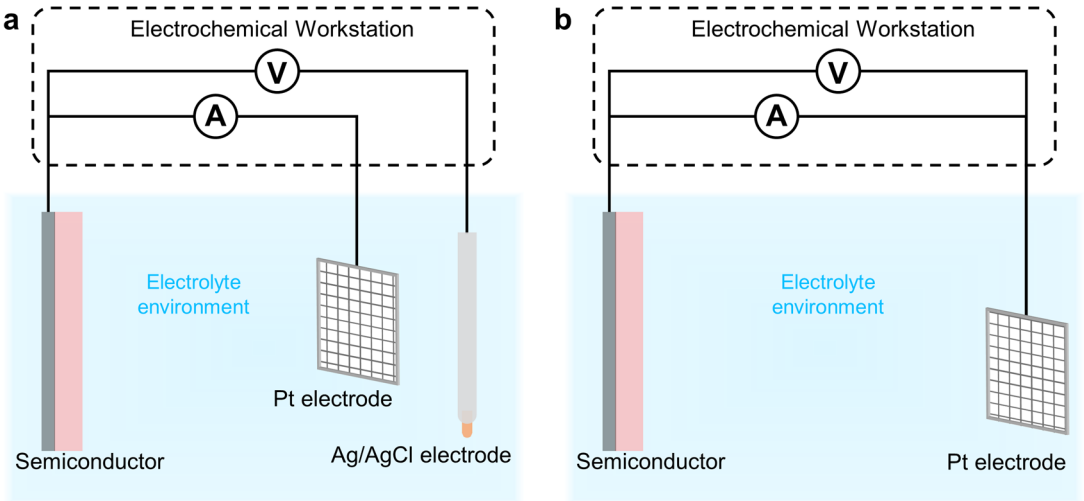

Supplementary Figure 2. Comparison of different testing configurations. (a) Schematic of the typical three-electrode configuration. (b) Schematic of the typical two-electrode configuration.

In photoelectrochemical devices, two different measurement setups are typically employed: three-electrode configuration and two-electrode configuration. As shown in Supplementary Figure 2a, the three-electrode configuration consists of a semiconductor photoelectrode, a Pt counter electrode, and an Ag/AgCl reference electrode. In this

configuration, the potential of the semiconductor electrode is measured relative to that of the Ag/AgCl electrode. The semiconductor electrode and the Pt counter electrode form the current loop. In contrast, the two-electrode configuration includes only the semiconductor photoelectrode and the Pt counter electrode. In this setup, the potential of the semiconductor photoelectrode is measured relative to that of the Pt electrode, and the semiconductor photoelectrode and the Pt electrode form the current loop. The three-electrode configuration has been commonly unitized as a diagnostic setup to evaluate the performance of photoelectrochemical devices[2]. Hence, we adopted the three-electrode configuration in our synaptic devices.

Supplementary Note 2. Comparison of working principles and device functionalities with previous studies

According to prior studies, semiconductor-based synaptic devices predominantly comprise solid-state and electrolyte-gated synapses. Solid-state devices encompass two-terminal and three-terminal synaptic devices (Supplementary Figure 3a). Given that our photoelectrochemical synapse and electrolyte-gated synapse both involve charge carrier (hole/electron behaviors) and ion-associated behaviors emulating biological synapses, different from conventional solid-state synapses, our main focus here is on the operation principles of electrolyte-gated devices and their distinction from our device. Electrolyte-gated devices primarily include electric-double-layer transistors (EDLT) and organic electrochemical transistor (OECT).

As depicted in Supplementary Figure 3b, in EDLT[3], which employs electrolyte as the gate dielectric, cations or anions accumulate at the electrolyte/semiconductor channel interface when a gate voltage is applied. This induces opposite charge carriers in the channel, altering the channel conductivity. Upon removing the gate voltage, the cation or anions in the electrolyte gradually revert to their initial positions due to the concentration gradient within the electrolyte, causing the electric-double-layer to dissipate and the channel conductivity to slowly recover. Different from the EDLT, which forms a capacitor at the interface, in the OECT (Supplementary Figure 3c), ions directly penetrate the semiconductor, altering the doping level throughout the channel and hence the conductivity[4].

The operation principle of our device differs significantly from those of solid-state devices, EDLT, and OECT (Supplementary Table 1). In photoelectrochemical synapse, the photoexcited charge carriers in the semiconductor undergo redox reactions with the ions and molecules in the electrolyte. Additionally, the semiconductor remains in its unaltered state without ion doping. This contrasts with the capacitance formation in EDLT and the ionic doping in OECT. Therefore, our device manifests device characteristics that are not reported, such as dual-modal synaptic plasticity, introduction of chemical modifications, electrolyte-regulated synaptic behaviors, and emulation of intricate biological phenomena.

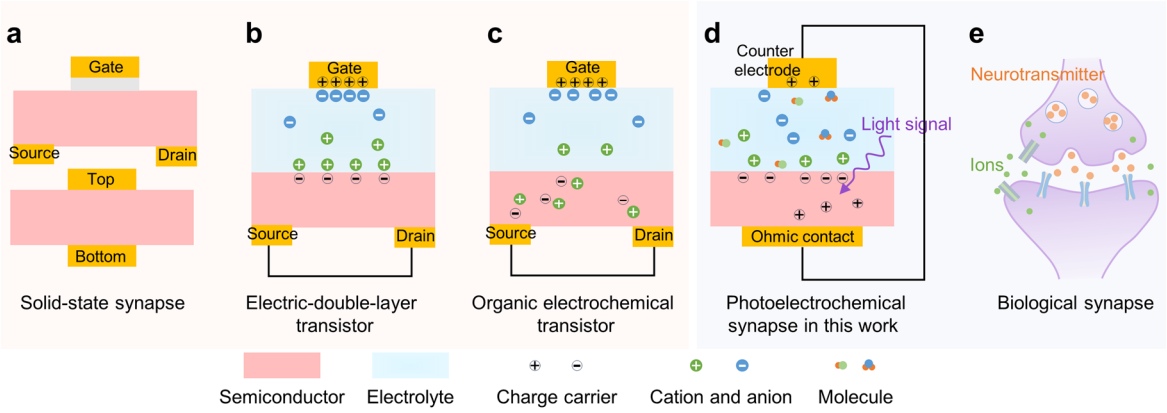

Supplementary Figure 3. Comparison of different types of semiconductor-based synapses and biological synapse. (a) Schematic of solid-state synapses including two-terminal (bottom) and three-terminal (top) device. (b-e) Schematic of electric-double-layer transistor (b), organic electrochemical transistor (c), photoelectrochemical synapse (d), and biological synapse (e).

Supplementary Table 1. Comparison of different types of semiconductor-based synapses

Device type	Device configuration	Electrolyte compatibility	Operation mechanism
Solid-state	Two or three-terminal	No	Diverse working mechanisms
EDLT	Three-terminal	Yes	Interface electric-double-layer capacitor modulation
OECT	Three-terminal	Yes	Ion penetration induced semiconductor doping
Photoelectrochemical synapse	**Two-terminal**	**Yes**	**Interface redox reaction and internal photoexcited carrier accumulation**

For synaptic devices, besides the neuromorphic computing field, many studies focus on the bionic functionalities and applications, which is also the focus of our work. To illustrate the differences between our device and previous works, as well as the novelty of our study, we conducted detailed discussion. Specifically, we analyzed and compared our work with previous studies in three aspects, primarily focusing on device structures and functional applications.

A. Comparing with previous neuromorphic devices with electrolyte-mediated processes

Previous neuromorphic devices with electrolyte-mediated processes, such as organic electrochemical transistors, fluidic memristors, and other novel devices, are typically employed for developing electrical synapses, optoelectronic synapses, and the incorporation of chemical-electric processes into electrical synapses, as summarized in Supplementary Table 2. In contrast, our proposed synaptic device, based on photoelectrochemical structure, manifests distinctive dual-modal synaptic plasticity and rich chemical-related functionalities through the interplay of chemical-electric and photo-electric synaptic processes, providing a novel platform for the advancement of multifunctional optoelectronic synapses.

B. Comparing with previous GaN-based synapses

We compare our work with previously reported GaN-based synaptic devices (Supplementary Table 3). Previously reported GaN-based synaptic devices typically employ either transistor structure with three terminals or electrode-semiconductor-electrode structure with two terminals, leveraging the photoelectric or piezoelectric effect of GaN to construct optoelectronic synapses or strain-sensitive electrical synapses, which do not involve chemical regulation process. In contrast, we propose a synaptic architecture based on photoelectrochemical structure and incorporate chemical-electric processes into optoelectronic synapse, leading to the demonstration of dual-modal plasticity and rich chemical-related functions, offering expanded applications for GaN materials in the field of constructing optoelectronic synapse.

C. Comparing with previous photoelectrochemical devices

Photoelectrochemical devices have been widely investigated but primarily utilized for photodetection and biosensing. Recent developments in photodetection involve photodetectors with multi-wavelength discrimination capability, which have been applied in optical

communication and logic gates[5,6]. In the field of biosensing, the photoelectrochemical strategy exhibits high sensitivity and low background noise, facilitating the detection of various biological substance such as DNA and tumor markers[7]. However, the potential application of photoelectrochemical structure in neuromorphic devices remains largely unexplored. The photoelectrochemical architecture allows for the introduction of chemical-electric processes into optoelectronic synapses, thus expanding their potential application. Moreover, in our future work, we aim to further enhance the device functionalities and applications of photoelectrochemical synapses by leveraging the well-established photoelectrochemical applications including multi-wavelength detection and biosensing.

Supplementary Table 2. Comparison of various electrolyte-mediated neuromorphic devices

Materials	Device type	Stimuli	Functionalities and applications	Ref.
PimB-Confined Channel	Fluidic memristor	Electrical, chemical	Chemical-regulated plasticity, chemical-electric signal transduction	[8]
n-type OMIEC	OECT	Electrical, chemical	ANN simulation, dopamine neuromorphic sensing	[9]
Azo-tz-PEDOT:PSS	OPECT	Light, electrical	Visual pathway mimicking, optoelectronic synaptic memory	[10]
Fiber PEDOT:PSS	OECT	Electrical, chemical	Dopamine-dependent plasticity	[11]
PEDOT:PSS	OECT	Electrical, chemical	Selective modulation of plasticity by glucose	[12]
PEDOT:PSS	OECT	Electrical, chemical	Dopamine-mediated plasticity, biohybrid synapse	[13]
Hydrogel	Ionic diode	Electrical	Dendritic signal integration	[14]
Graphene and CaF_2	Chemimemristor	Electrical	Long-term memory	[15]
p-AlGaN/n-GaN	**Photoelectrochemical**	**Light, electrical, chemical**	**Dual-modal synaptic plasticity, surface chemical modification, chemical-regulated behavior**	**This work**

OMIEC, organic mixed ionic-electronic conductors; OECT, Organic electrochemical transistor; ANN, artificial neural network; Azo-tz-PEDOT:PSS, poly(3,4-ethylenedioxythiophene) polystyrene sulfonate (PEDOT:PSS) covalently bonded to azobenzenes moieties; OPECT,

organic photoelectrochemical transistors;

Supplementary Table 3. Comparison between previous GaN-based synapses and photoelectrochemical synapse

Materials	Device structure	Stimuli	Functionality and application	Ref.
Perovskite-gated AlGaN/GaN	HEMT	Light, electrical	Gate-tunable synaptic behaviors, retinal cell simulation, image preprocessing and classification	[16]
AlGaN/GaN heterojunction	HEMT	Light, electrical	Optoelectronic logic gate	[17]
Si-doped GaN film	MSM	Light, electrical	Learning-experience behavior, visual recognition and memorization	[18]
GaN/AlN periodic structure	MSM	Light, electrical	Image information preprocessing	[19]
(Al,Ga)N nanowire	MSM	Light, electrical	Handwritten image recognition	[20]
GaN nanowire	MSM	Light, electrical	Learning-experience behavior, handwritten image recognition	[21]
AlGaN/GaN	HEMT	Light, electrical	Dual-synapse integration, letter recognition and classification	[22]
GaN microwire	MSM	Strain, electrical	Threshold switching behavior, short-term plasticity, piezotronic modulated plasticity	[23]
GaN nanowire	MSM	Electrical	Nonvolatile memristive behaviors, short-term plasticity	[24]
GaN Microwire	MSM	Strain, electrical	Multilevel switching capability, piezotronic modulated behaviors	[25]
GaN Microwire	MSM	Strain, electrical	Strain sensing and memorizing, haptic memory array	[26]
p-AlGaN/n-GaN nanowire	**Photoelectrochemical**	**Light, electrical, chemical**	**Dual-modal synaptic plasticity, surface chemical modification, visual memorization, chemical-regulated behaviors**	**This work**

HEMT, High-Electron-Mobility Transistor; MSM, metal-semiconductor-metal structure with two terminals

Supplementary Note 3. The importance of ion use, device biocompatibility, and its relevance to biological systems

A. Importance of ion use

The necessity of electrochemical reactions in ion environments is well-known for imitating biological neuron activity. For electrical synaptic devices, many significant works, which incorporate ion environments and ion-associated processes, have been reported to simulate neuromorphic functions, such as organic electrochemical transistors and fluidic memristors[8,27,28]. Compared to synaptic devices without ion processes, these devices exhibit unique advantages in the biohybrid field and mimicking chemical neuromorphic functionalities.

Recently, optoelectronic synaptic devices that integrate the photo-electric effect and synaptic plasticity have attracted significant attention, in which synaptic behaviors can be realized through mechanisms such as photogenerated carrier trapping without ion processes[29,30]. However, such operation mechanisms without the usage of ions may limit the potential of optoelectronic synapses for diverse tunability and multifunctional applications. Specifically, by introducing an aqueous working environment and ion/molecule-associated processes, new promising applications could be developed: 1) These optoelectronic synapses, operating within ion environments, hold promise for biohybrid applications, as demonstrated in previous studies[13], thereby facilitating the realization of optical brain-machine interfaces. 2) Furthermore, the incorporation of a chemical environment containing various ions and molecules can endow optoelectronic synapses with chemical-regulated and sensitive capabilities. Such feature not only aids in mimicking biorealistic visual systems with chemical-regulated processes but also offers the potential for multimodal sensing of both visual and chemical cues, thus broadening the application scope of existing optoelectronic synapses. Therefore, it is crucial to develop optoelectronic synapses with ion processes. In our study, we employ a photoelectrochemical configuration to introduce an electrolyte working environment and ion/molecule-related processes within optoelectronic synapses, leading to the demonstration of dual-modal synaptic plasticity and rich chemical-regulated synaptic behaviors.

B. Connection between our study and biological ion reactions

In biological systems, neural information transmission at synapses primarily involves ion-associated and neurotransmitter-associated processes. Ion-associated processes predominantly involve the efflux or influx of Na^+, K^+, and Cl^- ions through ion channels, leading to excitatory or inhibitory neuronal activities, while neurotransmitter-associated processes encompass the release, transmission, binding to postsynaptic receptors, and subsequent recycling or degradation of neurotransmitters. Due to the complexity of biological systems and the intrinsic working principles of artificial electronic devices, for artificial devices, it is quite challenging to exactly replicate the species and behaviors of ions and molecules found in biological systems. Although the ion processes and species in these devices differ significantly from those in biological systems, recent studies have exhibited that artificial synaptic devices with ion processes exhibit excellent neuromorphic functionalities and can successfully mimic biorealistic feedback systems. For instance, in organic electrochemical transistors, an electrolyte serves as the gate dielectric. When a gate voltage is applied, ions in the electrolyte penetrate the channel, altering the doping level and conductivity, thereby achieving synaptic

function[27,31]. In hydrogel-based devices, light or electrical stimuli are employed to facilitate ion movement and release (e.g., azo-benzene functionalized imidazole ions), which modulate ionic conductivity to emulate synaptic function and biological behaviors[14,32]. In our device, ions and molecules in the electrolyte environment (e.g., protons and ascorbic acid) undergo redox reactions with photogenerated electrons/holes at the electrolyte/semiconductor interface, which show diverse chemical-regulated synaptic behaviors. In our view, replicating biological ion reactions and mechanisms within synaptic devices is highly significant. This idea has been preliminarily exhibited by recent studies on fluidic memristor[8], which mimic ion channels and achieve synaptic behavior through hysteretic ion transport, thereby emulating chemical-related functions. However, considering that this field is still in its early stages, the primary focus of recent researches has not been on mimicking real biological ion reactions. Additionally, constructing such systems is quite challenging and requires interdisciplinary collaboration, which will be our goal in future endeavors.

Regarding the relevance of our device to biological systems, we elaborate as follows: 1) While the ion reaction within our device primarily involves protons, the electrolyte environment of our device is PBS solution (physiological electrolyte), which containing Na^+, K^+, and Cl^- ions, identical with biological systems. In the future, we will explore the use of Na^+, K^+, and Cl^- ions to replace protons to achieve synaptic responses. 2) The semiconductor/electrolyte junction in our device is inspired by the intracellular/extracellular form in biological systems. Based on such configuration, inspired by transmembrane receptors that connect extracellular and intracellular events, synaptic responses can be amplified by applying chemical modifications to nanowire surfaces, which tune external and internal charge behaviors. 3) Furthermore, we add H_2O_2 and ascorbic acid into our device, both of which involve physiological functions in biological systems. These molecules also exert synaptic modulation effects within our device, demonstrating chemically-regulated synaptic activities and oxidative stress-related behaviors induced by increased H_2O_2 concentration similar to those observed in biological systems.

C. Biocompatibility of our device

In our study, phosphate buffered saline (PBS) solution is used as the working environment for the photoelectrochemical synapse, which is a physiological electrolyte and widely used in biological experiments[33]. GaN and AlGaN possess excellent biocompatibility and biosafety, which have been used for bone regeneration[34]. Moreover, photoelectrochemical devices have been utilized for in vivo biosensing[35]. Overall, both the working environment and materials of our device are biocompatible. And studies on in vivo biosensing with photoelectrochemical devices have been reported, thus suggesting that the photoelectrochemical synapse is promising for constructing biohybrid systems. In our future work, we aim to realize a closed-loop neuromorphic systems which involve the interactive communications between the photoelectrochemical synapse and biological cells.

Supplementary Note 4. Working mechanism validation based on other nanowire samples and device structure

A. The necessity of p-n junction

To validate the working mechanisms, we prepared additional nanowire samples, including p-GaN directly grown on n-Si substrate (p-GaN/n-Si) and n-GaN directly grown on n-Si substrate (n-GaN/n-Si). Based on the working principles, the p-GaN/n-Si with an internal p-n junction would demonstrate both PSC and PSV responses, whereas the n-GaN/n-Si, lacking a p-n junction, is anticipated to only exhibit PSV response under open-circuit conditions. As shown in Supplementary Figure 4, our experimental results are consistent with the predictions, confirming the feasibility of our proposed mechanism. Moreover, above studies reveal the importance of p-n junction for synaptic responses in the current mode.

Interestingly, for the p-GaN/n-Si sample, before and after the Pt modification, the synaptic responses differ significantly. This phenomenon could be attributed to the nanowire surface being unsuitable for charge consumption by the electrolyte. Therefore, for the pristine nanowires, the internal p-n junction predominates, resulting in a large positive spike in the postsynaptic current curve (a significant negative spike in the postsynaptic voltage curve). With Pt modification, the charge transfer and consumption at the electrolyte surface is greatly promoted, exhibiting a noticeable suppression of the spike.

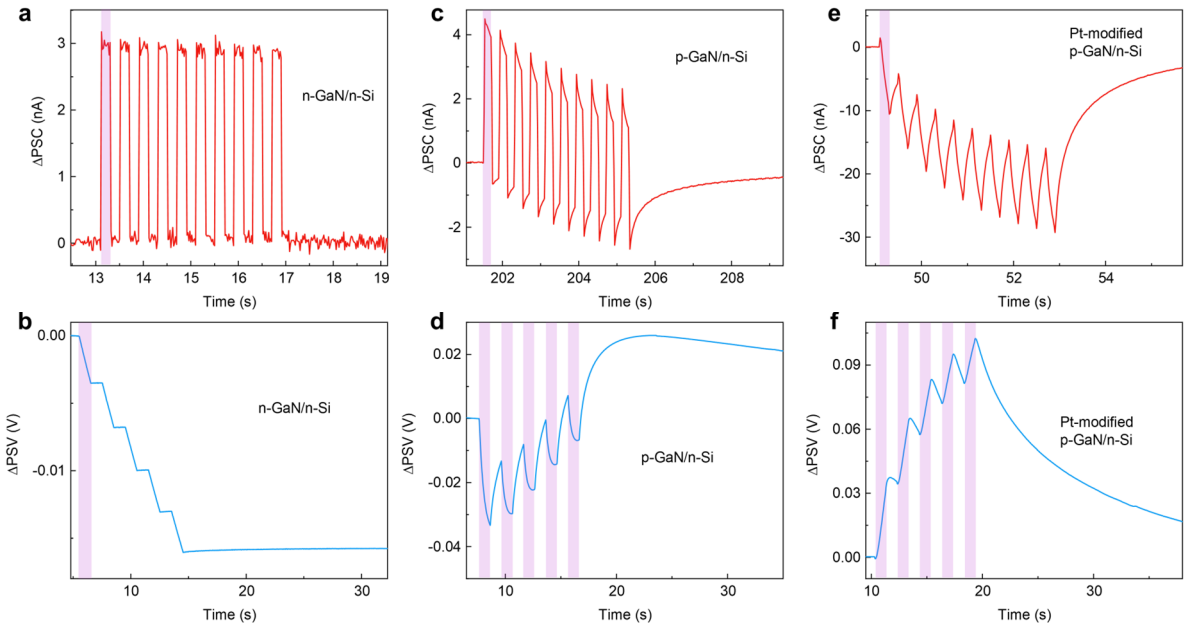

Supplementary Figure 4. Synaptic responses of different nanowire samples. (a, b) Optoelectronic responses of n-GaN/n-Si sample in current mode (a) and voltage mode (b). (c, d) Synaptic responses of p-GaN/n-Si sample in current mode (c) and voltage mode (d). (e, f) Synaptic responses of p-GaN/n-Si sample with Pt modification in current mode (e) and voltage mode (f). The purple block represents the light pulse of 340 nm. The light intensity is 28 μW cm^{-2}.

B. The necessity of semiconductor/electrolyte junction

To further illustrate the necessity of the electrolyte/semiconductor junction, we fabricated

solid-state devices using p-AlGaN/n-GaN nanowires and tested the photoresponse, as shown in Supplementary Figure 5. The solid-state device exhibits typical photodetector behaviors due to the p-n junction. In the photoelectrochemical synapse, the electrolyte environment creates a downward surface band bending at the p-AlGaN/electrolyte interface, thereby introducing two opposite built-in electric fields for carrier storage and synaptic behaviors.

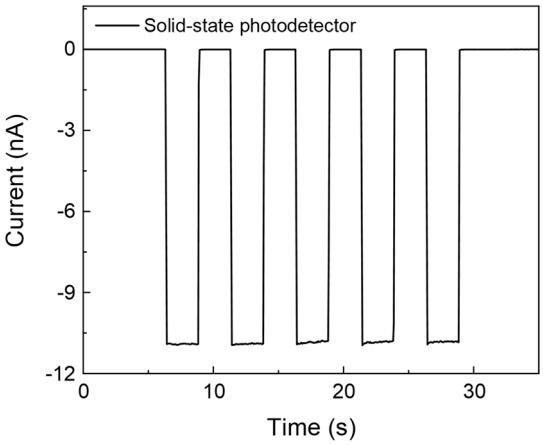

Supplementary Figure 5. Solid-state device. Photocurrent response of solid-state device based on p-AlGaN/n-GaN nanowires. Light pulses of 255 nm were used.

C. Rational control of the p-n junction length

To illustrate the necessity of controlling the length of p-n nanowire, we additionally prepare p-n junction nanowires, maintaining the length of p-AlGaN while increasing the length of n-GaN segment to 200 nm. The test results are depicted in Supplementary Figure 6. It is observed that compared to nanowires with 20 nm n-GaN segment, increasing the length of n-GaN substantially enhances the positive current peak in PSC mode. Correspondingly, in PSV mode, it leads to significantly large negative voltage peaks, resulting in unclear curve shapes that are difficult to distinguish. Under illumination, both the p-AlGaN and the 200 nm n-GaN segment absorb light, leading to more electrons flowing to the semiconductor, thereby resulting in significant peaks and unclear results. Therefore, besides introducing two back-to-back built-in electric fields (i.e., p-n junction and semiconductor/electrolyte junction) to achieve carrier storage, we need to rationally control the length of p-n junction to regulate synaptic behaviors.

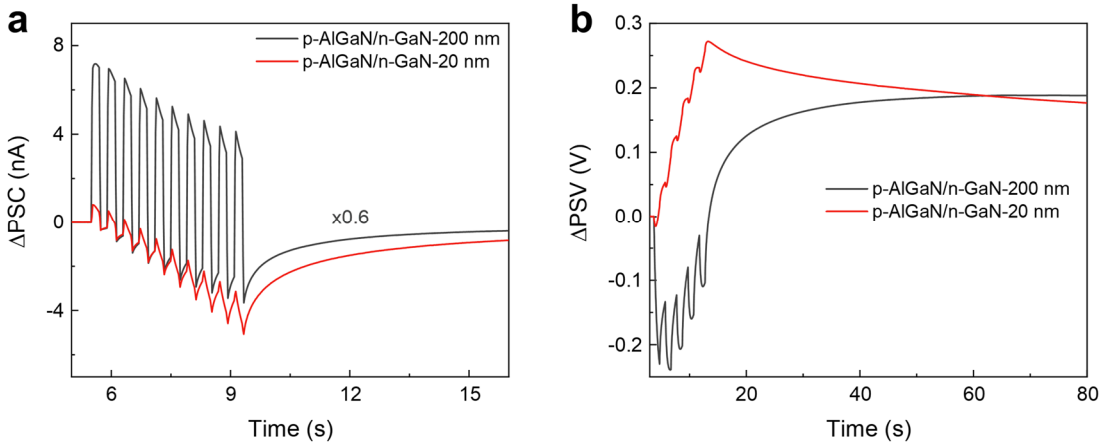

Supplementary Figure 6. Synaptic response of p-n nanowire with different length. (a, b) Postsynaptic current (a) and postsynaptic voltage (b) responses with different lengths of GaN

segment (All tests conducted in PBS solution). Light pulses of 255 nm and 12 μW cm^{-2} were used.

D. Discussion on the interplay of photo-electric and chemical-electric processes

1) The photo-electric process is indispensable; without it, our device cannot achieve the functions related to optoelectronic synapses.

2) To underscore the significance of the chemical-electric process, we fabricated a solid-state photodetector using p-AlGaN/n-GaN nanowires, with Ni/Au and Ti/Au employed for ohmic contacts. The photoresponse behavior is depicted in Supplementary Figure 5, showcasing typical photodetector responses attributed to the p-n junction structure. In our photoelectrochemical synapse, the introduction of an electrolyte environment induces downward surface band bending at the p-AlGaN/electrolyte interface, thereby introducing two opposite built-in electric fields within the device. These fields facilitate carrier storage and synaptic behaviors, which distinct from the rapid response, thereby highlighting the necessity of chemical-electric process.

3) In the manuscript, by changing pulse parameters such as duration and number, and adjusting the electrolyte environment by introducing chemical molecules, the synaptic response of the device can be altered, indicating the interplay of the photo-electric and chemical-electric processes, which collectively govern the synaptic response.

Supplementary Note 5. The quantitative comparison of the photo-electric and chemical-electric processes

The discussion regarding the quantitative analysis of photo-electric and chemical-electric processes is as follows:

A. Time constants of photo-electric and chemical-electric processes

1) The internal photo-electric processes mainly involve the transfer of photogenerated electrons towards electrolyte or external circuit, as well as the storage and dissipation of photogenerated holes. The transfer of electrons within the semiconductor occurs in the time range of ~10^{-9} s[36], whereas hole dissipation requires much longer time due to the interface barrier, which take at least ~10^{2} s to decay to the initial state[37].

2) The external electrolyte-mediated chemical-electric processes involve the dissipation of electrons and holes by the electrolyte with the time scale of ~10^{-3} s[36]. Note that these time constants are provided for reference only. Considering our device operates in aqueous environment, the photo-electric and chemical-electric processes are closely connected, making it challenging to measure the specific time required for above two processes. In future work, we will attempt to conduct in-situ time-resolved analyses to study the time-resolved charge carrier dynamics of the distinctive synaptic behaviors.

B. Detailed analysis in our device from illumination to dark conditions

Upon illumination, photogenerated electrons flow towards the electrolyte and external circuit. Owing to the slower transfer and consumption processes of electrons at the electrolyte interface (~10^{-3} s) compared to transfer processes within the semiconductor (~10^{-9} s), photogenerated electrons inevitably flow towards the external circuit first, leading to the initial spike observed in the curve. Even though loading Pt accelerates the chemical reaction at the interface, it is still slower than the carrier transport within the semiconductor[36]. This inevitably leads to a small number of electrons flowing to the external circuit through the p-n junction, manifested as the small positive PSC peak observed at the initial stage. Upon cessation of illumination, stored holes dissipate slowly (~10^{2} s), which is much longer than the time required for electron transfer and chemical reactions in the electrolyte (~10^{-3} s). Hence, the recorded curves exhibit a slow relaxation over time. Moreover, in PSC mode, charge carriers can be consumed through both internal circuit and external electrolyte pathways, while the carriers in PSV mode can only dissipate through the external solution, leading to different time dependencies between the two modes (Supplementary Figure 7).

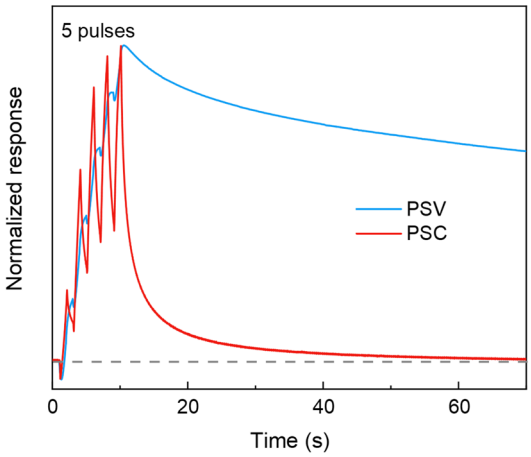

Supplementary Figure 7. Normalized synaptic responses in the two modes. The same optical stimulation was utilized, with both pulse duration and interval set to 1 s. Light pulses of 255 nm and 12 μW cm^{-2} were used.

Supplementary Note 6. Cycle-to-cycle and device-to-device variations

We conducted additional tests to assess cycle-to-cycle and device-to-device variations of the photoelectrochemical synapses in voltage and current modes. In the current mode, we compared the peak values after 10 pulses, while in the voltage mode, we compared the peak values after 5 pulses. All test results are summarized in Supplementary Figure 8. Here, the variation is defined as the ratio of the standard deviation to the mean. For cycle-to-cycle variation, we tested 30 cycles. In the voltage mode, the variation is 1.54%, whereas it is 3.08% in the current mode. During the long-term testing, a slight performance decline is observed. To enhance the long-term stability, protective coatings can be employed on the nanowire surface in future work. Regarding device-to-device variation, we prepared 10 devices. In the voltage mode, the variation is 3.29%, and it is 3.04% in the current mode. In future research, we can further enhance device uniformity by utilizing selective area growth to improve nanowire uniformity.

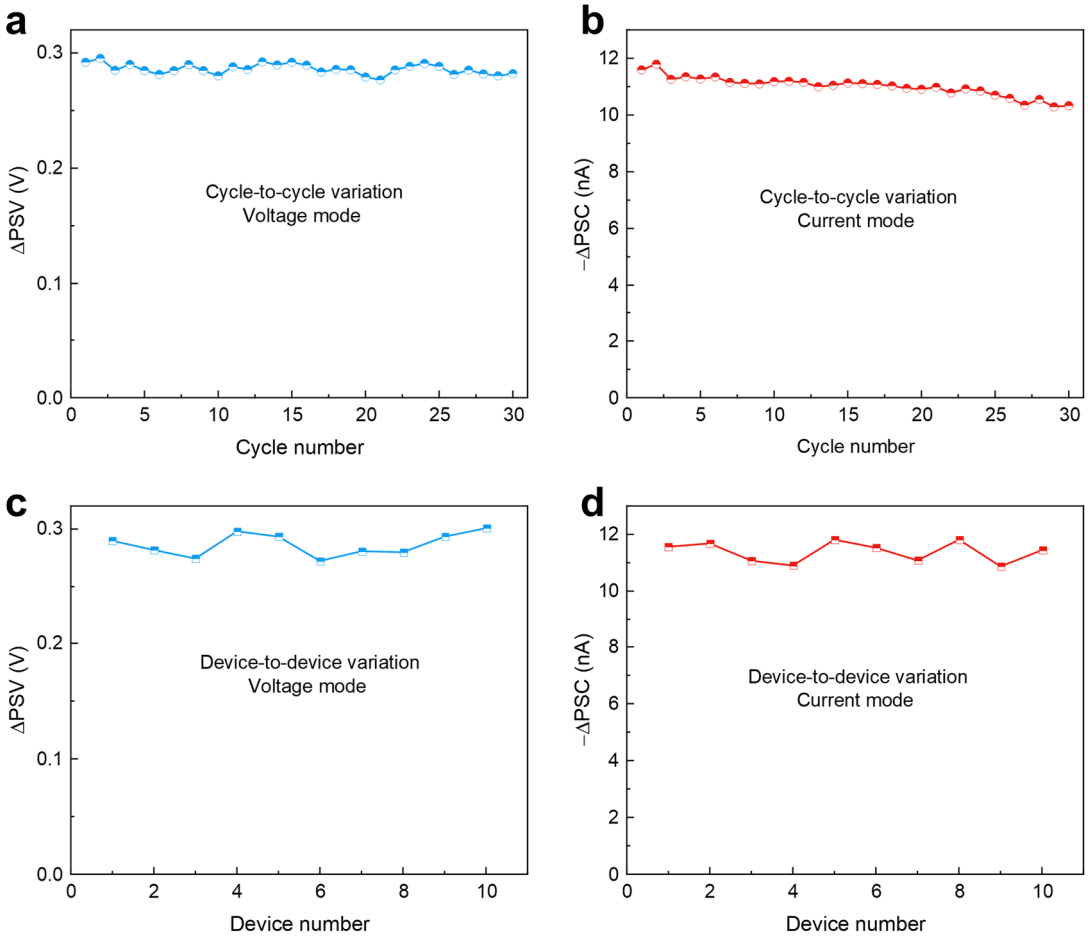

Supplementary Figure 8. Cycle-to-cycle and device-to-device variation of the photoelectrochemical synapse. (a, b) Cycle-to-cycle variation in voltage mode (a) and current mode (b). (c, d) Device-to-device variation in voltage mode (c) and current mode (d). In current mode, 10 pulses of optical stimulation were utilized, with both duration and interval set to 0.2 s. In voltage mode, 5 pulses of optical stimulation were utilized, with both duration and interval set to 1 s. We compared the peak values after light stimuli to investigate the variations. Light pulses of 255 nm and 12 μW cm^{-2} were used.

Supplementary Note 7. Current (voltage) signal polarity definition and electric field discussion

The photoelectrochemical device operates in either current or voltage mode, with the electrical response signals exhibiting opposite polarities in each mode, as illustrated in Supplementary Figure 9a and b. The relationship between the direction of charge carrier movement and the polarity of current (voltage) in our device is described as follows: (1) In current mode, when electrons flow towards the electrolyte, the current is negative; when electrons move towards the semiconductor and external circuit, the current is positive. (2) In voltage mode, electron movement towards the electrolyte produces a positive voltage spike, while electron movement towards the semiconductor leads to a negative voltage spike.

The electric fields in our device involve the electrolyte/p-AlGaN and p-AlGaN/n-GaN junctions, as shown in Supplementary Figure 9c.

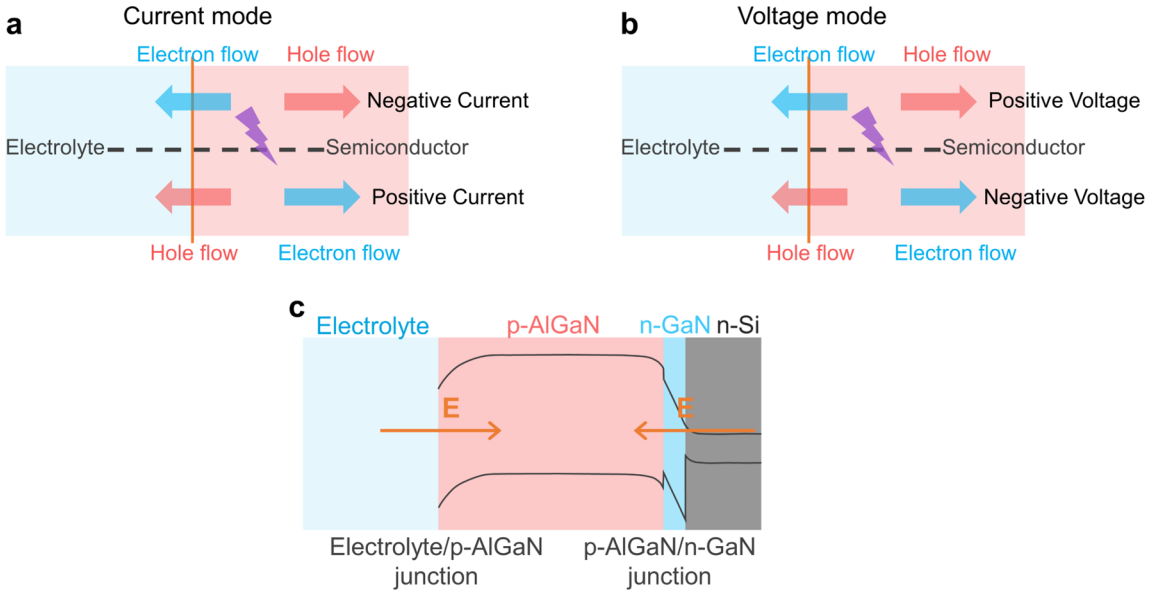

Supplementary Figure 9. Response polarity definition and electric field description. (a, b) Schematic illustrations of the polarity definitions for postsynaptic current (a) and postsynaptic voltage (b) in the photoelectrochemical synapse. (c) Schematic of the built-in electric fields, indicating the opposite directions of the two fields.

Supplementary Note 8. Detailed processes of the chemical-electric behavior

(1) Interface redox reaction between electron/hole in p-AlGaN and aqueous electrolyte:

1.1) Mechanism analysis of redox reaction: As shown in Supplementary Figure 10, the conduction and valence band edges of AlGaN straddle water redox potentials. When p-AlGaN is immersed in an aqueous electrolyte and exposed to light above the bandgap, the photogenerated electrons and holes separate, transport, are then consumed by the aqueous electrolyte. These electrons flow into the electrolyte to undergo hydrogen generation reactions ($4e^- + 4H^+ \rightarrow 2H_2$), while holes flow to the Pt electrode to undergo oxygen generation reactions ($4h^+ + 2H_2O \rightarrow O_2 + 4H^+$). Such phenomenon has been widely demonstrated and discussed in previous researches[1,38]. Additionally, GaN-based materials including InGaN, GaN, and AlGaN have been widely used for hydrogen and oxygen generation via water splitting[1,38]. GaN-based nanowires grown by MBE, including InGaN, GaN, and AlGaN, have been extensively utilized for hydrogen and oxygen production in acidic environments, exhibiting excellent long-term stability[2,39]. GaN-based materials are highly stable in acidic environments and do not react with protons[40,41].

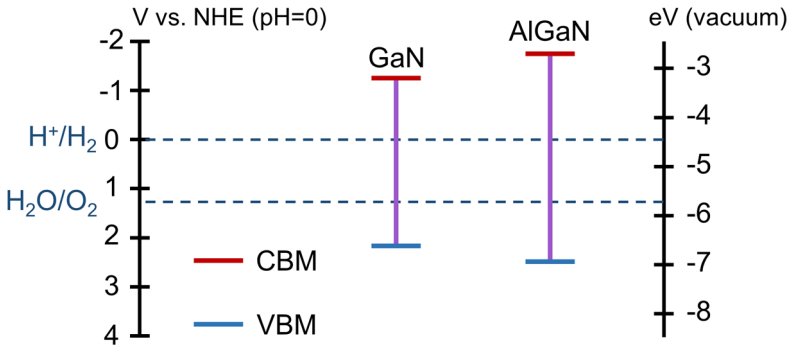

Supplementary Figure 10. Band structure. Schematic diagram of the GaN and AlGaN band structures.

1.2) Experimental evidence of redox reaction: In our device, when p-AlGaN is illuminated by photons with energy greater than the bandgap, photo-electric process occurs, generating charge carriers. These charge carriers separate, transport, and ultimately undergo redox reactions with the aqueous electrolyte, being consumed via water splitting to produce hydrogen and oxygen. However, in our tests, due to the small current of nA level and short duration of 10^2 s, the gas produced is at the order of 10^{-10} L. Considering the solubility of H_2 in water, which is approximately 1.83 ml H_2/100 ml, it is difficult to directly detect the generated hydrogen and oxygen in our regular tests. To further demonstrate the generation of hydrogen and oxygen, we increased the applied voltage and duration (i.e., extreme condition) to accumulate gas output. After both regular and extreme tests, we used inert argon (Ar) to purge the gases from the sealed chambers and collected them in gas bags. Then, we analyzed the collected gases using gas chromatograph (Agilent 8860 gas chromatograph). Before the gas chromatography tests, we cleaned the instrument with Ar. It should be noted that during the gas detection process, we collected the produced gases using gas bags and then injected the gases into the chromatograph for analysis, which is offline test. Inevitably, trace amounts of air might be introduced, including at the chromatograph's inlet. Supplementary Figure 11a shows the result after the regular test (0 V, 100 s), revealing signal peaks for O_2 and N_2, but none for H_2.

The absence of an H_2 signal is due to the extremely low gas production, while the observed O_2 and N_2 signals are mainly because trace amounts of air were introduced during the offline test process. To better illustrate the redox reactions occurring in the device (i.e., H_2 generation at the nanowire electrode and O_2 generation at the Pt electrode), we utilized an H-shaped cell for analysis. The nanowire electrode and Pt electrode were placed in two separate chambers, connected by a proton exchange membrane (Nafion 117 film). This type of cell is widely used in studies of hydrogen and oxygen production[42]. After the extreme test (-0.5 V, 1 h), we collected gases from each chamber using gas bags and performed gas chromatography analysis. For the nanowire electrode, a significant H_2 peak was observed, confirming the production of H_2 (Supplementary Figure 11b). Additionally, minor peaks for O_2 and N_2 were observed, which are consistent with the result under regular conditions and are attributed to the offline test process. For the Pt electrode, a significant O_2 peak was detected, with the intensity of the O_2 peak being much greater than that of the N_2 peak (Supplementary Figure 11c). Compared to the result in Supplementary Figure 11a, the O_2/N_2 intensity ratio is significantly different, which rules out the interference from the offline test process and confirms the production of O_2.

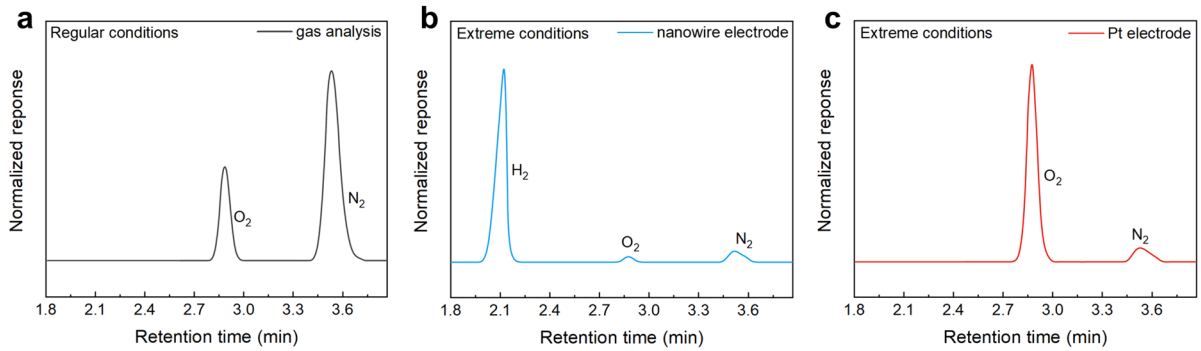

Supplementary Figure 11. Gas chromatography analysis. (a) Results under regular conditions (0 V, 100 s). (b, c) Results under extreme conditions (-0.5 V, 1 h).

(2) The influence of chemical changes on electron/hole consumption and electrical signals:

Altering the chemical environment of the electrolyte affects the redox reactions between electrons/holes and the electrolyte, thereby influencing the transport of electrons/holes to the external circuit and ultimately regulating device synaptic responses, as schematically illustrated in Supplementary Figure 12a. In our study, we focused on altering proton concentration (i.e., H_2SO_4 concentration and pH value), varying the concentration of conductive ions (Na_2SO_4 concentration), adding ascorbic acid, and adding H_2O_2. The detailed regulation mechanisms are as follows:

2.0) Default Condition: When the chemical environment of the electrolyte remains unchanged, electrons and holes are consumed through the redox reactions of water splitting. In our device, the semiconductor electrode determines the polarity and magnitude of the photoresponse. Therefore, we discuss the consumption of electrons and holes at the semiconductor/electrolyte interface. At the semiconductor/electrolyte interface, under default conditions, the primary chemical reaction involve electron consumption reaction ($4e^- + 4H^+ \rightarrow 2H_2$). This corresponds to holes flowing towards the circuit, which are recorded by the instrument as negative current. Moreover, a faster electron consumption rate (i.e., more holes

flowing to the circuit) corresponds to a larger negative current.

2.1) Proton Concentration: In the reaction between protons and electrons ($2e^- + 2H^+ \rightarrow H_2$), the concentration of protons significantly influences the reaction rate. As the proton concentration increases, the reaction between electrons and protons accelerates, leading to an increase in the negative current response[43,44]. Therefore, in our device, by adjusting the H_2SO_4 concentration and pH value to alter the proton concentration, the synaptic response of the device can be significantly regulated. As the H_2SO_4 concentration increases and the pH value decreases, the synaptic response of the device increases notably (Supplementary Figure 12b).

2.2) Conductive ions concentration: Increasing the concentration of conductive ions is equivalent to increasing the conductivity of electrolyte. The consumption rates of electrons and holes at the semiconductor/electrolyte interface both increase. In this context, the holes flowing to the external circuit decrease, resulting in a decrease in the negative current (Supplementary Figure 12b). Therefore, when water is replaced with Na_2SO_4 solution, the postsynaptic current decreases, which is consistent with previous report[43]. However, further increasing the Na_2SO_4 concentration has little effect. This may be explained by considering that the increased conductivity of the electrolyte solution no longer significantly impacts the synaptic performance, indicating that the influence of electrolyte conductivity has reached saturation.

3) Adding ascorbic acid (AA): AA, which is a common electron donor, can undergo oxidation reactions with holes ($AA + h^+ \rightarrow$ dehydro-ascorbic acid). This hole consumption reaction can easily happen, which is more favorable than the default hole consumption reaction[45,46]. Therefore, AA can capture holes and facilitates hole consumption at the semiconductor/electrolyte interface. As a result, the holes flowing to the external circuit decrease, leading to a decrease in synaptic responses (Supplementary Figure 12b).

4) Adding H_2O_2: H_2O_2 is widely used as hole scavenger ($H_2O_2 + 2h^+ \rightarrow O_2 + 2H^+$). This hole consumption reaction can easily happen, which is more favorable than the default hole consumption reaction[47,48]. In our device, H_2O_2 can capture holes and promotes hole consumption at the electrolyte/semiconductor interface and reduces the holes flowing to the external circuit, resulting in a decrease in the synaptic response (Supplementary Figure 12b). Note that although protons are generated when H_2O_2 is consumed, the electrolyte used is PBS buffer solution, and the pH of the solution remains constant (i.e., the proton concentration remains unchanged).

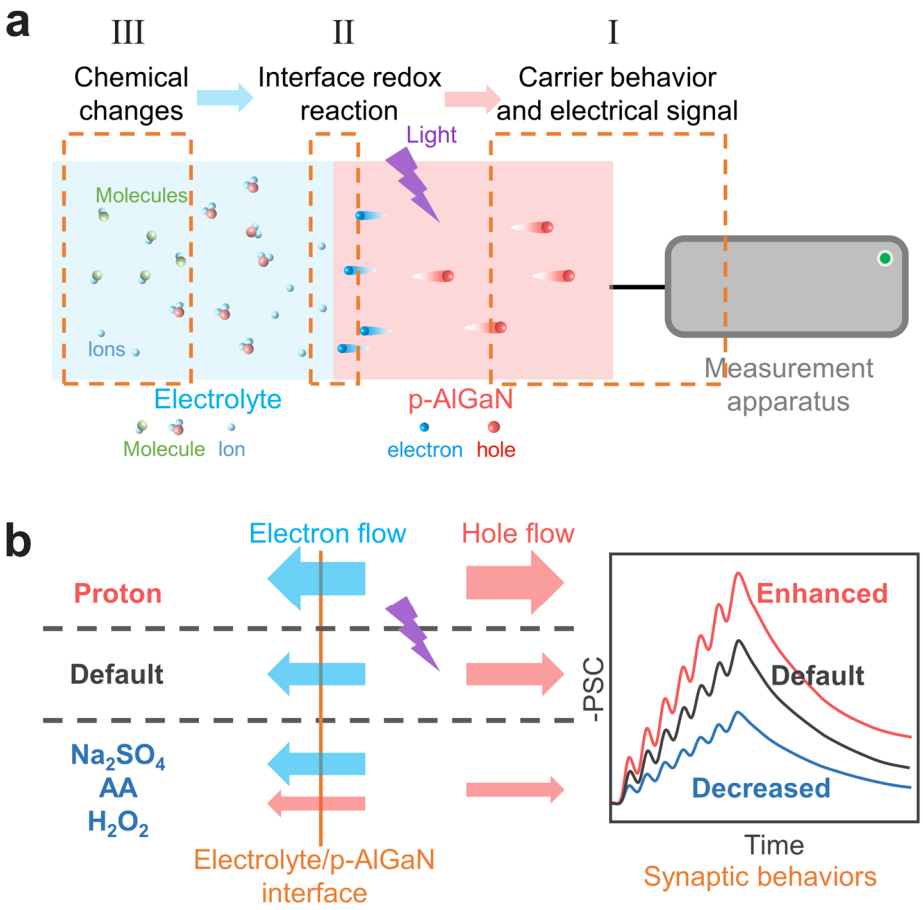

Supplementary Figure 12. Influence of chemical changes. (a) Schematic diagram illustrating the chemical-electric process at the p-AlGaN/electrolyte interface. (b) Schematic illustrating the impact of changing chemical environments on synaptic responses. "Default" refers to the default electrolyte environment without changing the chemical surroundings.

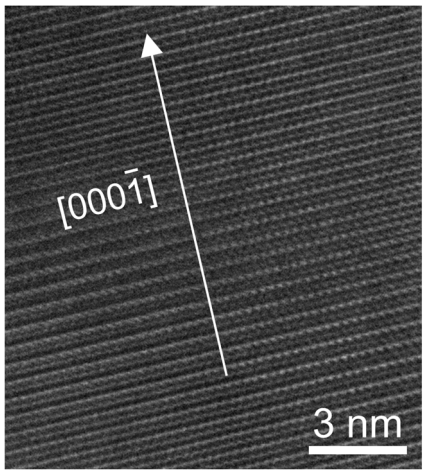

Supplementary Figure 13. HRTEM image. High-resolution TEM image, showing excellent crystallinity of MBE-grown nanowire.

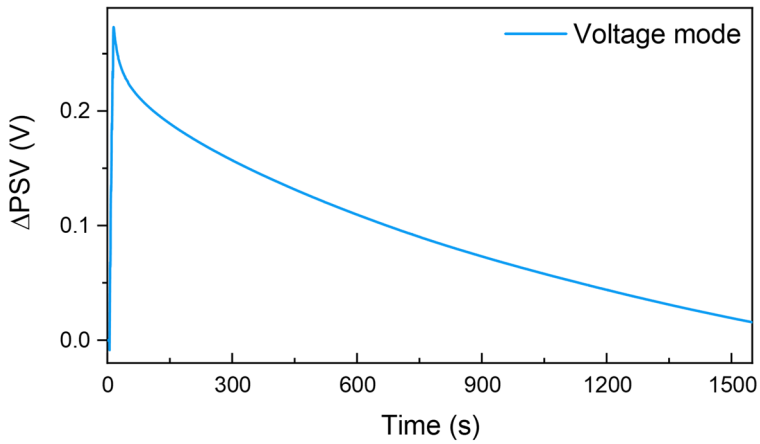

Supplementary Figure 14. Postsynaptic voltage response. Postsynaptic voltage response of pristine nanowires. Five optical pulses were applied, with both duration and interval set to 1 s. Light pulses of 255 nm and 12 μW cm^{-2} were used.

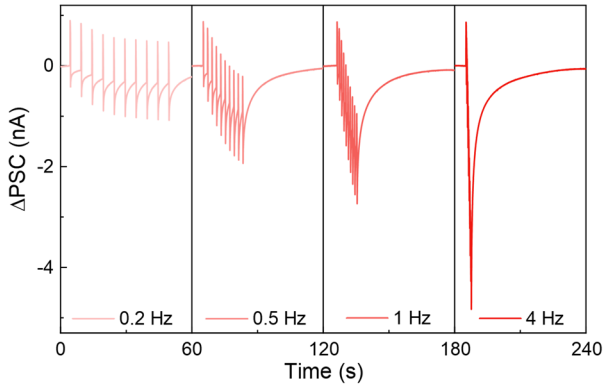

Supplementary Figure 15. The correlation between ΔPSC and pulse frequencies. The synaptic response increases with the frequency increasing. The pulse width is 0.2 s and the light pulse of 12 μW cm^{-2} is used.

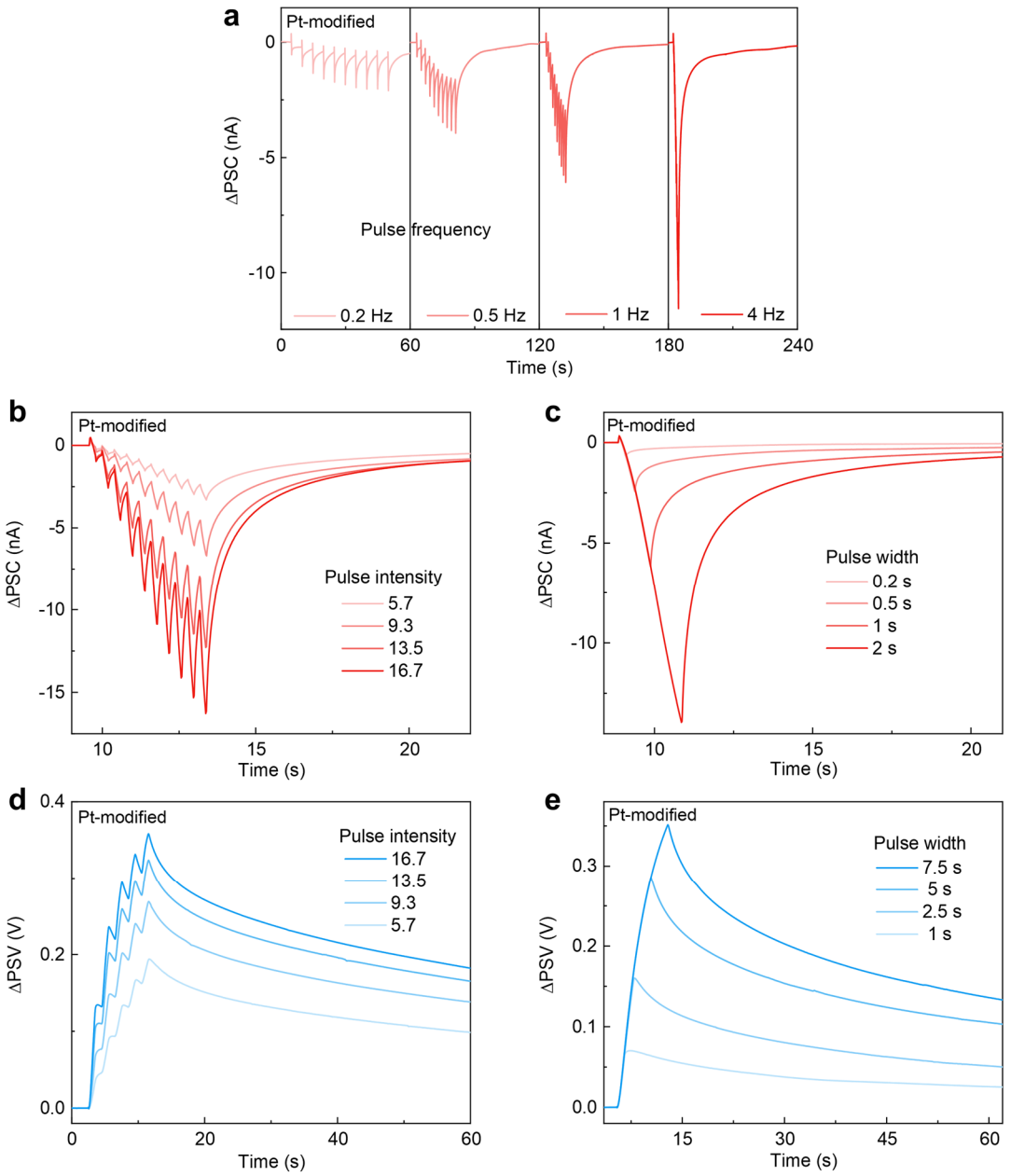

Supplementary Figure 16. Synaptic responses under different pulse conditions. (a-c) Synaptic responses with different pulse frequencies (a), pulse intensities (b), pulse widths (c) in current mode. (d-e) Synaptic responses with different pulse intensities (d) and pulse widths (e) in voltage mode. The inset numbers in (b) and (d) represent different light intensities from 5.7 to 16.7 μW cm^{-2}.

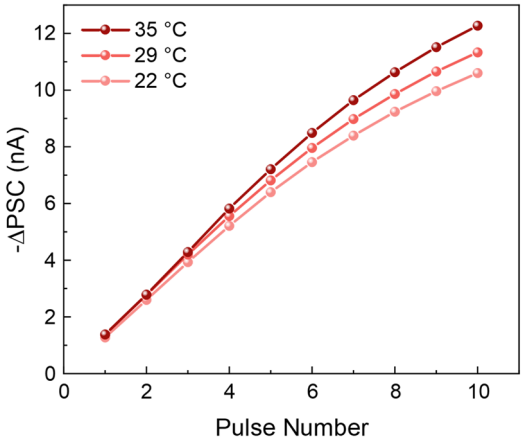

Supplementary Figure 17. Synaptic response of the photoelectrochemical synapse at different electrolyte temperatures. With the temperature increasing, the synaptic response increases. Light pulses of 255 nm and 12 μW cm^{-2} were used. Note that we take the absolute value of the postsynaptic current (-ΔPSC) for performance comparison.

Supplementary References:

1. Kibria, M. G. et al. Visible light-driven efficient overall water splitting using p-type metal-nitride nanowire arrays. *Nat. Commun.* **6**, 6797 (2015).
2. Xiao, Y. et al. Oxynitrides enabled photoelectrochemical water splitting with over 3,000 hrs stable operation in practical two-electrode configuration. *Nat. Commun.* **14**, 2047 (2023).
3. Wang, D. et al. Recent advanced applications of ion-gel in ionic-gated transistor. *npj Flexible Electron.* **5**, 13 (2021).
4. Rivnay, J. et al. Organic electrochemical transistors. *Nat. Rev. Mater.* **3**, 1–14 (2018).
5. Chen, W. et al. Manipulating Surface Band Bending of III-Nitride Nanowires with Ambipolar Charge-Transfer Characteristics: A Pathway Toward Advanced Photoswitching Logic Gates and Encrypted Optical Communication. *Adv. Mater.* **36**, 2307779 (2024).
6. Wang, D. et al. Bidirectional photocurrent in p–n heterojunction nanowires. *Nat. Electron.* **4**, 645–652 (2021).
7. Shu, J.&Tang, D. Recent Advances in Photoelectrochemical Sensing: From Engineered Photoactive Materials to Sensing Devices and Detection Modes. *Anal. Chem.* **92**, 363–377 (2020).
8. Xiong, T. et al. Neuromorphic functions with a polyelectrolyte-confined fluidic memristor. *Science* **379**, 156–161 (2023).
9. Liu, R. et al. Versatile Neuromorphic Modulation and Biosensing based on N-type Small-molecule Organic Mixed Ionic-Electronic Conductors. *Angew. Chem. Int. Ed.* **136**, 202315537 (2024).
10. Corrado, F. et al. Azobenzene-based optoelectronic transistors for neurohybrid building blocks. *Nat. Commun.* **14**, 6760 (2023).
11. Alarcon-Espejo, P. et al. High Hole Mobility Fiber Organic Electrochemical Transistors for next-Generation Adaptive Neuromorphic bio-Hybrid Technologies. *Adv. Mater.* **36**, 2305371 (2024).
12. Xu, X. et al. An Aqueous Electrolyte Gated Artificial Synapse with Synaptic Plasticity Selectively Mediated by Biomolecules. *Angew. Chem. Int. Ed.* **62**, 202302723 (2023)
13. Keene, S. T. et al. A biohybrid synapse with neurotransmitter-mediated plasticity. *Nat. Mater.* **19**, 969–973 (2020).
14. Han, S. H., Kim, S. I., Oh, M. A.&Chung, T. D. Iontronic analog of synaptic plasticity: Hydrogel-based ionic diode with chemical precipitation and dissolution. *Proc. Natl Acad. Sci. USA* **120**, 2211442120 (2023).
15. Wang, Y. et al. Aqueous chemimemristor based on proton-permeable graphene membranes. *Proc. Natl Acad. Sci. USA* **121**, 2314347121 (2024).
16. Hong, X. et al. Two-Dimensional Perovskite-Gated AlGaN/GaN High-Electron-Mobility-Transistor for Neuromorphic Vision Sensor. *Adv. Sci.* **9**, 2202019 (2022).
17. Kai, C. et al. AlGaN/GaN-Based Optoelectronic Synaptic Devices for Neuromorphic Computing. *Adv. Optical Mater.* **11**, 2202105 (2023).
18. Mo, Y., Luo, B., Dong, H.&Hou, B. Light-stimulated artificial synapses based on Si-doped GaN thin films. *J. Mater. Chem. C* **10**, 13099 (2022).
19. Hua, X. et al. Artificial Optoelectronic Synapse with Nanolayered GaN/AlN Periodic Structure for Neuromorphic Computing. *ACS Appl. Nano Mater.* **6**, 8461–8467 (2023).
20. Gu, X. et al. Realize ultralow-energy-consumption photo-synaptic device based on a single

(Al,Ga)N nanowire for neuromorphic computing. *Nano Res.* **17**, 1933–1941 (2024).
21. Zhou, M. et al. Light-stimulated low-power artificial synapse based on a single GaN nanowire for neuromorphic computing. *Photonics Res.* **11**, 1667–1677 (2023).
22. Chang, K.-C. et al. Optoelectronic Dual-Synapse based on Wafer-level GaN-on-Si Device Incorporating Embedded SiO2 Barrier Layers. *Nano Energy* **125**, 109564 (2024).
23. Hua, Q. et al. Piezotronic Synapse Based on a Single GaN Microwire for Artificial Sensory Systems. *Nano Lett.* **20**, 3761−3768 (2020).
24. Huang, C. H., Wu, C. Y., Lin, Y. F., Chou, Y. C.&Lee, K. T. Wet-Etching-Boosted Charge Storage in 1D Nitride-Based Systems for Imitating Biological Synaptic Behaviors. *Adv. Funct. Mater.* **33**, 2306030 (2023).
25. Liu, H. et al. A Bamboo-Like GaN Microwire-Based Piezotronic Memristor. *Adv. Funct. Mater.* **26**, 5307–5314 (2016).
26. Hua, Q. et al. Flexible GaN microwire-based piezotronic sensory memory device. *Nano Energy* **78**, 105312 (2020).
27. Gkoupidenis, P. et al. Organic mixed conductors for bioinspired electronics. *Nat. Rev. Mater.* **9**, 134–149 (2024).
28. Emmerich, T. et al. Nanofluidic logic with mechano–ionic memristive switches. *Nat. Electron.* **7**, 271–278 (2024).
29. Liu, K. et al. An optoelectronic synapse based on α-In2Se3 with controllable temporal dynamics for multimode and multiscale reservoir computing. *Nat. Electron.* **5**, 761–773 (2022).
30. Ilyas, N. et al. Nanostructured Materials and Architectures for Advanced Optoelectronic Synaptic Devices. *Adv. Funct. Mater.* **32**, 2110976 (2022).
31. Harikesh, P. C. et al. Organic electrochemical neurons and synapses with ion mediated spiking. *Nat. Commun.* **13**, 901 (2022).
32. Tian, H. et al. Optically modulated ionic conductivity in a hydrogel for emulating synaptic functions. *Sci. Adv.* **9**, eadd6950 (2023).
33. Li, Y. et al. Efficient Killing of Multidrug-Resistant Internalized Bacteria by AIEgens In Vivo. *Adv. Sci.* **8**, 2001750 (2021).
34. Zhang, C. et al. A Novel Approach to Enhance Bone Regeneration by Controlling the Polarity of GaN/AlGaN Heterostructures. *Adv. Funct. Mater.* **31**, 2007487 (2021).
35. Wang, X. et al. A Photoelectrochemical Sensor for Real-Time Monitoring of Neurochemical Signals in the Brain of Awake Animals. *Anal. Chem.* **96**, 6079–6088 (2024).
36. Yang, W. et al. Time-Resolved Observations of Photo-Generated Charge-Carrier Dynamics in Sb2Se3 Photocathodes for Photoelectrochemical Water Splitting. *ACS Nano* **12**, 11088 (2018).
37. Han, X. et al. Response Speed-Tunable Photodetectors Based on Hybrid Ternary FePSe3 Nanoflakes. *Adv. Optical Mater.* **11**, 2300317 (2023).
38. Zhou, P. et al. Solar-to-hydrogen efficiency of more than 9% in photocatalytic water splitting. *Nature* **613**, 66–70 (2023).
39. Dong, W. J. et al. Pt nanoclusters on GaN nanowires for solar-asssisted seawater hydrogen evolution. *Nat. Commun.* **14**, 179 (2023).
40. AlOtaibi, B. et al. Highly stable photoelectrochemical water splitting and hydrogen generation using a double-band InGaN/GaN core/shell nanowire photoanode. *Nano Lett.* **13**, 4356–4361 (2013).

41. Ding, X. et al. Molecular gated-AlGaN/GaN high electron mobility transistor for pH detection. *Analyst* **143**, 2784–2789 (2018).
42. Ta, X. M. C. et al. Alternatives to Water Photooxidation for Photoelectrochemical Solar Energy Conversion and Green H2 Production. *Adv. Energy Mater.* **12**, 2201358 (2022).
43. Wang, D. et al. Observation of polarity-switchable photoconductivity in III-nitride/MoSx core-shell nanowires. *Light: Sci. Appl.* **11**, 227 (2022).
44. Fang, J. et al. Photobase effect for just-in-time delivery in photocatalytic hydrogen generation. *Nat. Commun.* **11**, 5179 (2020).
45. Xu, X. et al. Ascorbic acid as an effective antioxidant additive to enhance the efficiency and stability of Pb/Sn-based binary perovskite solar cells. *Nano Energy* **34**, 392–398 (2017).
46. Saha, S., Yang, J., Masouleh, S. S. M., Botton, G. A.&Soleymani, L. Hot hole direct photoelectrochemistry of Au NPs: Interband versus Intraband hot carriers. *Electrochim. Acta* **404**, 139746 (2022).
47. Chu, S. et al. Solar Water Oxidation by an InGaN Nanowire Photoanode with a Bandgap of 1.7 eV. *ACS Energy Lett.* **3**, 307–314 (2018).
48. Kamimura, J. et al. Broad Band Light Absorption and High Photocurrent of (In,Ga)N Nanowire Photoanodes Resulting from a Radial Stark Effect. *ACS Appl. Mater. Interfaces* **8**, 34490–34496 (2016).